PHYSICAL SCIENCES

Single-particle surface-enhanced coherent anti–Stokes Raman scattering: Nanoparticle design and mechanism

Sanjun Fan[1]*†, Ran Cheng[2]†, Haonan Lin[3]†, Zhewen Luo[4], Abigail E. Smith[1], Chih-Feng Wang[5], Jinna He[6], Brian T. Scarpitti[1], Deben N. Shoup[1], Hannah C. Schorr[1], Erjun Liang[7], Jian Ye[4], Ji-Xin Cheng[3]*, Zachary D. Schultz[1]*

Surface-enhanced coherent anti–Stokes Raman scattering (SECARS) is believed to increase the signal intensity and sensitivity by combining the localized surface plasmon resonance and coherent Raman enhancement. However, the realization of SECARS is more complex than for surface-enhanced Raman scattering (SERS) and remains challenging. Unlike SERS, the nonlinear CARS process requires the coherent interaction of three distinct fields. The interactions between the electric fields and nanoparticle (NP) morphology for single-particle SECARS remain unexplored, and the underlying mechanisms generating the SECARS signal are not fully understood. Here, 27 distinct NPs were synthesized and screened using a CARS microscope. Among them, only star-core core-satellite NPs show single-particle SECARS signals, which were affected by laser polarization, two-photon luminescence background, photoinduced heating effects, particle size, and particle morphology. The influence of NP properties on SECARS enhancement offers guidance for the design and synthesis of NPs for single-particle SECARS and opportunities in biological imaging and chemical sensing.

INTRODUCTION

Raman spectroscopy is widely used to probe the molecular structure and composition of materials with minimal sample preparation and is applicable to a broad range of disciplines, from material science and chemistry to biology, forensic science, and medicine. Nevertheless, the small Raman cross-section on the level of $\sim 10^{-30}$ cm^2 sr^{-1} results in an intrinsically weak signal that can limit its utility in certain applications (*1*). Surface-enhanced Raman scattering (SERS) is a highly sensitive analytical tool that leverages the enhancement of the electromagnetic field near metal surfaces, typically gold (Au) or silver (Ag) nanoparticles (NPs), to detect and identify low concentrations of chemical and biological analytes (*2*, *3*). The electromagnetic field enhancement near the NP surface allows SERS to achieve high sensitivity, whereas achieving acquisition rates faster than ~10 Hz in the single- or few-molecule limit is considered challenging (*4*, *5*). Surface-enhanced coherent Raman scattering (SECRS), including surface-enhanced stimulated Raman scattering (SESRS) and surface-enhanced coherent anti–Stokes Raman scattering (SECARS), offers a promising alternative to break the speed limit imposed by SERS (*6*), which can improve the imaging speed by orders of magnitude due to the introduction of coherent Raman enhancement (*7*, *8*). In addition, the plasmonic enhancement can also contribute to the greater sensitivities, enabling single-molecule SECRS detection with a pixel acquisition time of a microsecond and below (*9*–*12*).

The continuous development of diverse plasmonic nanostructures has been fueling the advancements of SECARS since its first demonstration on a flat Ag film in 1979 (*13*). Film-based plasmonic substrates are widely used to experimentally boost SECARS signals, with broad genres spanning plain Au films with (*14*) or without (*15*) Au or silicon (Si) particles, dielectric films with Au particles (*10*, *16*), nanostructured Au or Ag surfaces (*17*, *18*), plasmonic Doppler gratings (*19*), graphene with Au pyramids (*20*), graphene oxide (*21*), self-assembled silica microspheres on polymer grating samples (*22*), and glass substrates with randomly dispersed or self-assembled Au NPs (*23*–*25*) or Si-based nanoantennas (*26*). Theoretically, film-based substrates provide more flexibility for morphological modifications via sophisticated nanofabrication, which leads to highly tunable surface plasmon resonances that match with both the pump and Stokes excitation wavelengths and anti-Stokes emission wavelength, thus enabling the strongest signal enhancement (*27*–*31*). However, similar to SERS, one limitation of film-based substrate enhancements lies in their reliance on near-field effects, which only amplify signals from analytes located in extremely close proximity to the plasmonic surface. This requirement for intimate contact restricts their applicability in biological contexts, such as bioimaging. For example, cellular imaging has been enhanced with a thin Au film, but the cells were dried prior to imaging so that the cellular components could be close to the Au surface (*32*), which hinders its potential for studying living cells or micron-thick biopsies.

Plasmonic NPs open opportunities for SECARS to be applied for bioimaging because they can be targeted to distinct locations in biological samples. By functionalizing the plasmonic NPs with Raman-active indicators, SECARS nanotags are encoded by the indicators and present bright SECARS signals for detection. When combining SECARS probes with protein-based stabilizers or targeting motifs, SECARS has broadened its biomedical applications to high-speed cellular imaging (*33*) and examining pathological biopsy via immunohistochemistry (*34*). Current applications of SECARS nanotags have used Au nanospheres, relying on simple dimerization (*9*, *35*, *36*) or passive clustering in cells or tissue (*33*, *34*) to create "hotspots" that generate bright SECARS signals. The electromagnetic enhancement factor (EF) for SECARS is theorized

[1]Department of Chemistry and Biochemistry, The Ohio State University, Columbus, OH 43210, USA. [2]Department of Chemistry, Boston University, Boston, MA 02215, USA. [3]Department of Electrical and Computer Engineering and Department of Biomedical Engineering, Boston University, Boston, MA 02215, USA. [4]School of Biomedical Engineering, Shanghai Jiao Tong University, Shanghai 200030, China. [5]Physical Sciences Division, Pacific Northwest National Laboratory, Richland, WA 99352, USA. [6]School of Electric and Mechanical Engineering, Pingdingshan University, Pingdingshan 467000, China. [7]School of Physics and Laboratory of Zhongyuan Light, Zhengzhou University, Zhengzhou 450001, China.
*Corresponding author. Email: fan.1113@osu.edu (S.F.); jxcheng@bu.edu (J.-X.C.); schultz.133@osu.edu (Z.D.S.)
†These authors contributed equally to this work.

to be higher than that for SERS due to its higher-order dependence on incidence power and enhancement from anti-Stokes photons (*37*). However, in reality, the generation of SECARS signal from a single plasmonic NP is more challenging than SERS due to (i) the involvement of light at three distinct wavelengths (i.e., pump, Stokes, and anti-Stokes); (ii) acquisition times for SECARS that are three orders or more shorter than SERS; (iii) the generation of nonresonant background from processes like two-photon luminescence (TPL) or four-wave mixing (FWM) background from Au NPs (*25*, *38*), dependent on different excitation conditions; (iv) experimental EFs several orders of magnitude lower than expected theoretical EFs observed in clustered plasmonic nanostructures (*23*, *24*, *39*); and (v) coherent interference between fields originating within a plasmonic junction (*9*). Some of these factors can be addressed, for example, the nonresonant background can be suppressed using time-resolved surface-enhanced coherent anti–Stokes Raman scattering (tr-SECARS) spectroscopy (*24*) or wide-field FWM microscope (*40*, *41*). However, many of these complications remain puzzling. Despite the design and optimization of plasmonic NPs for single-particle SECARS performance, only Au nanodumbbells consisting of a Au NP dimer inside a silica shell have been explored for single-particle SECARS (*9*, *35*, *36*), and plasmonic NPs with other morphologies have not been successfully reported.

As shown in Fig. 1, we synthesized diverse shapes of NPs, including spheres, rods, stars, bipyramids, gap-enhanced Raman tags (GERTs), intragap or porous NPs, dimers, core/shell particles, and core-satellite (CS) particles. We then screened these NPs using a hyperspectral CARS microscope to quickly acquire the average SECARS signals over a large region, from which we identified the NPs with SECARS signals. Next, we performed single-particle SECARS examinations on numerous individual NPs, whose single-particle identities were confirmed via colocalized scanning electron microscopy (SEM) (*25*). We found among all the NPs screened that only star-core CS NPs showed single-particle SECARS signals. Through the study of different star-core CS NPs, experimental results showed that single-particle SECARS signal was greatly affected by laser polarization, TPL background, photoinduced heating effects, and the plasmonic properties of star-core CS NPs such as the number of hotspots, sizes, shapes, and aggregates. We further compared SERS and SECARS at the single-particle level with simulations to validate our experimental results. The results indicate that certain NPs, such as Au nanospheres, may fail to produce detectable SECARS signals due to lower overall enhancement, whereas CS NPs exhibiting the strongest electromagnetic field enhancement are detected by SECARS.

RESULTS

NP preparation

We synthesized a variety of NPs shown in Fig. 2 and then screened them using a CARS microscope to quickly evaluate their SECARS signals in a 40,000-μm^2 region. These NPs include Au nanospheres, isotropic/anisotropic nanostars, nanorods, bipyramids, nanorod/bipyramid-based intragap NPs, porous NPs, core/shell NPs, GERTs, and sphere/star-core CS NPs both with and without silica shell coatings, etc. To find optimal NPs that exhibit CARS signals from single NPs, we designed the localized surface plasmon resonance (LSPR) peaks to vary broadly across the visible and near-infrared (NIR) spectral range. The LSPR peaks of diverse NPs at 543 nm (GERTs), 544 nm (nanosphere), 578 nm (isotropic nanostars), 540 and 628 nm (core/shell), 517 and 723 nm (bipyramids), 581 and 863 nm (bigger core/shell), 520 and 874 nm (porous CS NPs), 820 and 931 nm (anisotropic nanostars), 506 and 1028 nm (nanorods), etc. were measured as shown in figs. S1 to S3. In addition, we synthesized silica shell–coated sphere-core CS NPs (sphere-core SiO_2-CS NPs) using a linker [11-mercaptoundecanoic acid (11-MUA) paired with polyethylenimine (PEI)], because this configuration creates nanogaps, or hotspots, between the core and satellites, which is believed to intensify the electromagnetic fields. First, as shown in fig. S4, we synthesized several different sizes of nanospheres, among which the nanospheres (50/70/90 nm) were used as cores and the nanospheres (12 and 20 nm) served as satellites. Second, two kinds of CS NPs [(50-12, 70-12, 90-12 nm) and (50-20, 70-20, 90-20 nm)] were then prepared as shown in fig. S5 and Fig. 2 (M to O), and their corresponding extinction spectra were shown in fig. S5. The size distribution of spherical and silica shell–coated CS NPs was shown in fig. S6 (G and H). With increased sizes of

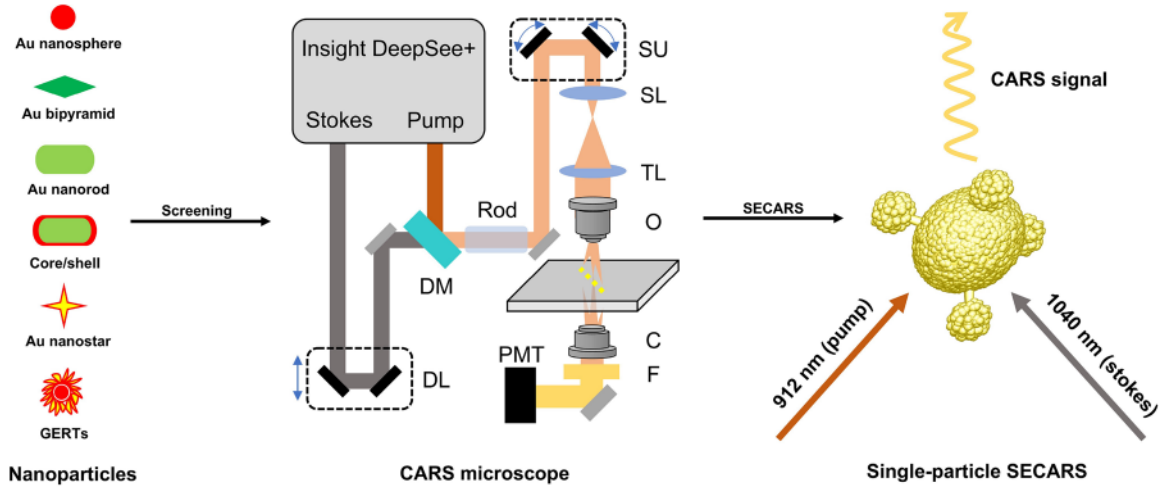

Fig. 1. Schematic diagram for single-particle SECARS measurement. A variety of NPs are screened using a CARS microscope, and then, single-particle SECARS signal is investigated using CS NPs. C, condenser; DL, delay line; DM, dichroic mirror; F, filter; O, objective; PMT, photomultiplier tube; SL, scan lens; SU, scanning unit; TL, tube lens.

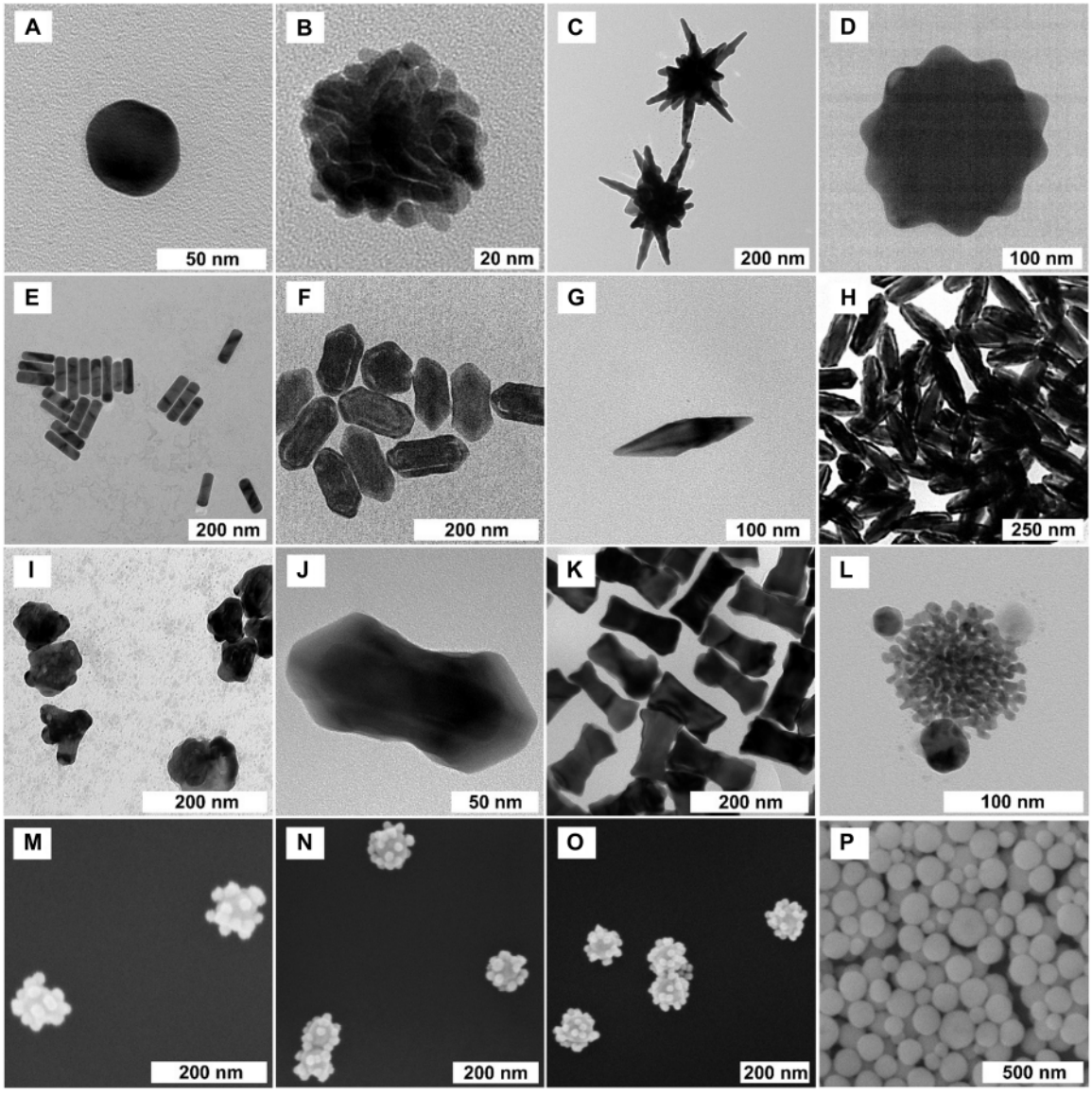

Fig. 2. Characterization of NPs. Transmission electron microscopy (TEM) images of (**A**) Au nanosphere, (**B**) GERTs (200 μl of 10 mM $HAuCl_4$), (**C**) anisotropic nanostars (20 μl of Au seed solution), (**D**) isotropic nanostar, (**E**) nanorods (0.6 ml of 10 mM $HAuCl_4$), (**F**) nanorod-based intragap NPs, (**G**) bipyramid (0.5 ml of seed solution), (**H**) bipyramid-based intragap NPs, (**I**) nanostar-based porous NPs, (**J**) core/shell NPs (via method 1 in the Supplementary Materials), (**K**) core/shell NPs via method 3 in the Supplementary Materials, and (**L**) porous Au star (core)/sphere (satellite) NP; SEM images of (**M**) 50-nm sphere (core)/20-nm sphere (satellite) NPs, (**N**) 70-nm sphere (core)/20-nm sphere (satellite) NPs, (**O**) 90-nm sphere (core)/20-nm sphere (satellite) NPs, and (**P**) silica shell–coated 70-nm sphere (core)/20-nm sphere (satellite) NPs.

cores and satellites, the LSPR peaks exhibited a red shift. For example, the silica shell–coated CS NPs in fig. S6 (D to F) show that the major peak at 678 nm red-shifts to 713 nm when the core size increases. Last, sphere-core SiO_2-CS NPs were obtained in Fig. 2P and fig. S6 with varied LSPR peaks within the region of 630 to 720 nm.

SECARS signal screening

We first screened 20 types (Fig. 2, A to L and P, and figs. S1F, S2, D and H, S3, and S6, A and D to F) out of 27 NPs prepared the NP preparation section under a CARS microscope to quickly evaluate their CARS signals by averaging the overall signals generated by NPs over the 40,000-μm^2 field of view. As shown in fig. S7, out of the 20 types of NPs with different morphologies, only bipyramid-based intragap NPs (fig. S7H), nanostar-based porous NPs (fig. S7I), and sphere-core SiO_2-CS NPs (Fig. 3, A to C) exhibited weak ensemble SECARS signals. However, no SECARS signal can be detected from them at the single-particle level, which suggests that the SECARS we observed from ensemble samples incorporates some level of interparticle coupling rather than from intrinsic single-particle enhancement (*42*). Regarding the sphere-core SiO_2-CS NPs, we found that the ensemble SECARS signals from 50-20 nm sphere-core SiO_2-CS NPs was higher than 50-12 nm sphere-core SiO_2-CS NPs (fig. S8), which was ascribed to both larger satellite sizes used and a main, red-shifted CS coupling LSPR peak at 678 nm of 50-20 nm sphere-core SiO_2-CS NPs. In addition, a new shoulder peak at 547 nm was observed for 50-20 nm sphere-core SiO_2-CS NPs due to interparticle

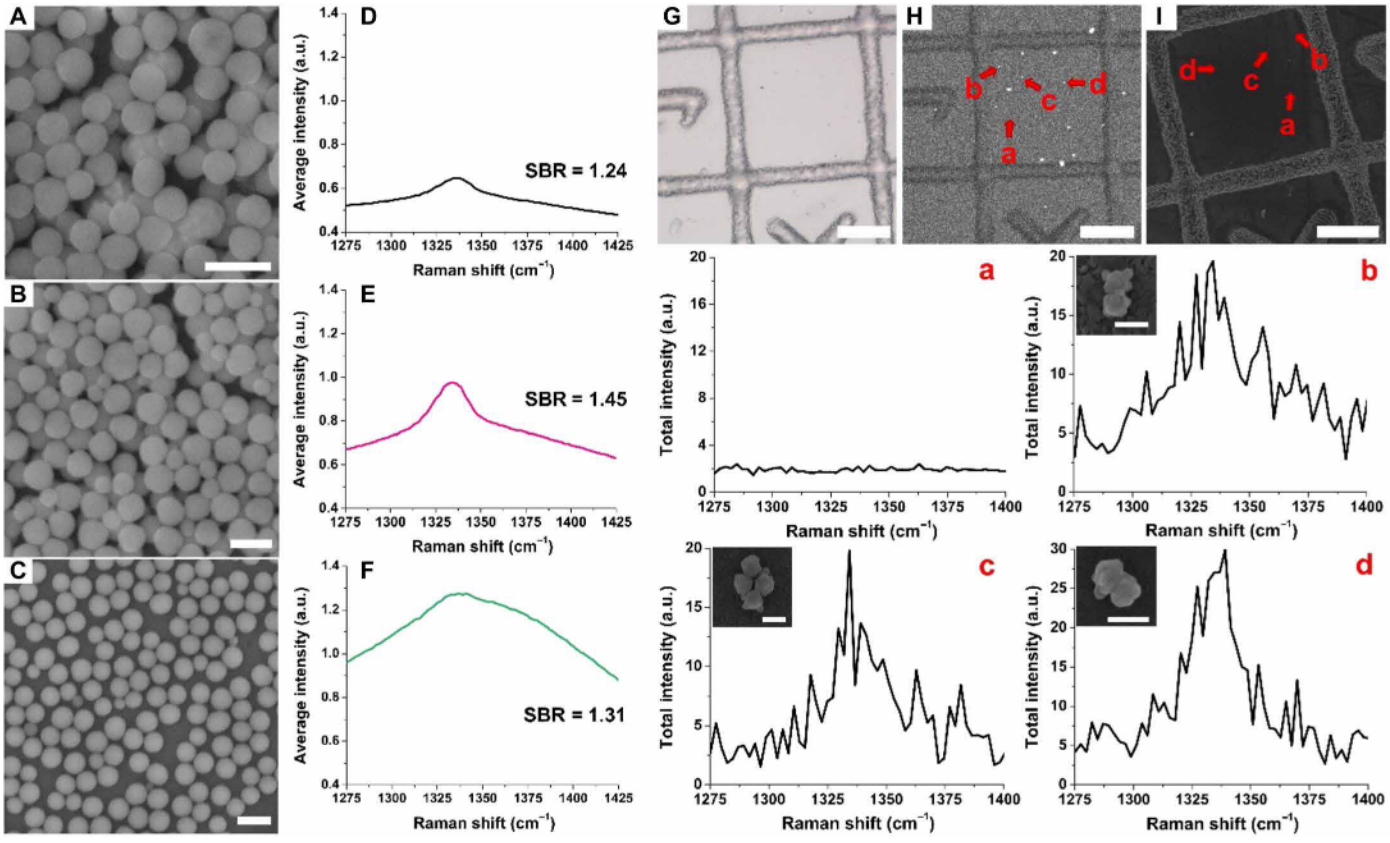

Fig. 3. SECARS signals of sphere-core SiO_2-CS NPs. Ensemble-averaged SECARS signals of sphere-core SiO_2-CS NPs (**A**) 50-20 nm, (**B**) 70-20 nm, and (**C**) 90-20 nm, measured across three distinct sample regions. Scale bars, 200 nm. Colocalized SECARS and SEM studies guided by a labeled glass substrate. (**D**) SECARS signal of NPs in (A). (**E**) SECARS signal of NPs in (B). (**F**) SECARS signal of NPs in (C). The signal to background ratio (SBR) is noted for (D to F). (**G**) A bright-field image of the photoetched glass substrate with labeled grids. The unlabeled grid in the center was defined as the ROI. Scale bar, 20 μm. (**H**) The averaged SECARS image of a hyperspectral imaging stack that covered the ROI. Scale bar, 20 μm. (**I**) SEM image of the same ROI. Scale bar, 20 μm. Below are SECARS spectra of the bare glass substrate without nanotag presented from location a, and nanotags presented at locations b to d. The corresponding nanostructures were shown by SEM images as the upper left insets. Scale bars, 200 nm. SECARS spectra (a to d) were collected at 600 × 600 pixels per frame with 60 sequential frames, a pixel size of 150 nm, and a pixel dwell time of 10 μs per pixel per frame and power set at 200 μW for both pump and Stokes beams. The intensities are noted in arbitrary units (a.u.).

coupling among satellites (fig. S6), contributing to the overall stronger plasmonic enhancement. We further explored whether increasing the size of cores could also help with the improvements of SECARS performances. We observed that as the core sizes increased, the TPL background rose substantially for the 70-20 nm and 90-20 nm sphere-core SiO_2-CS NPs (Fig. 3, D to F), most likely due to enhanced radiative damping, which commonly occurs in larger or resonant structures (*43*, *44*). The intensity ratios of the SECARS peak and the background increased when changing the core size from 50 to 70 nm but substantially decreased when core size increased to 90 nm. Based on these results, 70-20 nm sphere-core SiO_2-CS NPs were selected as the optimal candidate for single-particle SECARS examinations due to the highest signal-to-background ratio observed in the ensemble sample.

To perform the single-particle SECARS study, highly diluted 70-20 nm sphere-core SiO_2-CS NPs were drop-casted and dried on the photoetched glass substrate with 50-μm labeled grids as shown in Fig. 3G, where the labels served to identify the region of interest (ROI). SECARS hyperspectral imaging was first performed, by which SECARS spectra from nanostructures were obtained and NP distributions were simultaneously revealed by the average image of the whole hyperspectral imaging stack (Fig. 3H). SEM imaging was performed after SECARS on the exact same area (Fig. 3I). Notably, the SEM image and the SECARS image are mirror-symmetric to each other, as revealed by the photoetched labels. The SECARS spectrum of the bare glass substrate without nanotags present was measured at location a, and we observed a weak background without any distinct peak present. We also observed SECARS signals originating from b or d individual NPs when they were in close vicinity, as shown at location b and c or from an NP dimer wrapped in the same silica shell as shown at location d. Notably, there were no distinct SECARS signals observed from single NPs using silica shell–coated spherical CS NPs. However, these silica-coated particles provide important information to guide the design of NPs where star cores were used for single-particle SECARS.

Star-core CS NP synthesis, SECARS measurement, and simulations

Considering that the CS NP is a promising structure for single-particle SECARS, we therefore modified the morphology to further red-shift the LSPR and introduce more and stronger hotspots to enhance the SECARS signal. A linker-free method was developed to synthesize star-core CS NPs (*45*), avoiding the usage of linkers such as PEI or DNA. As shown in Fig. 4 (A to G), the satellite spheres continuously

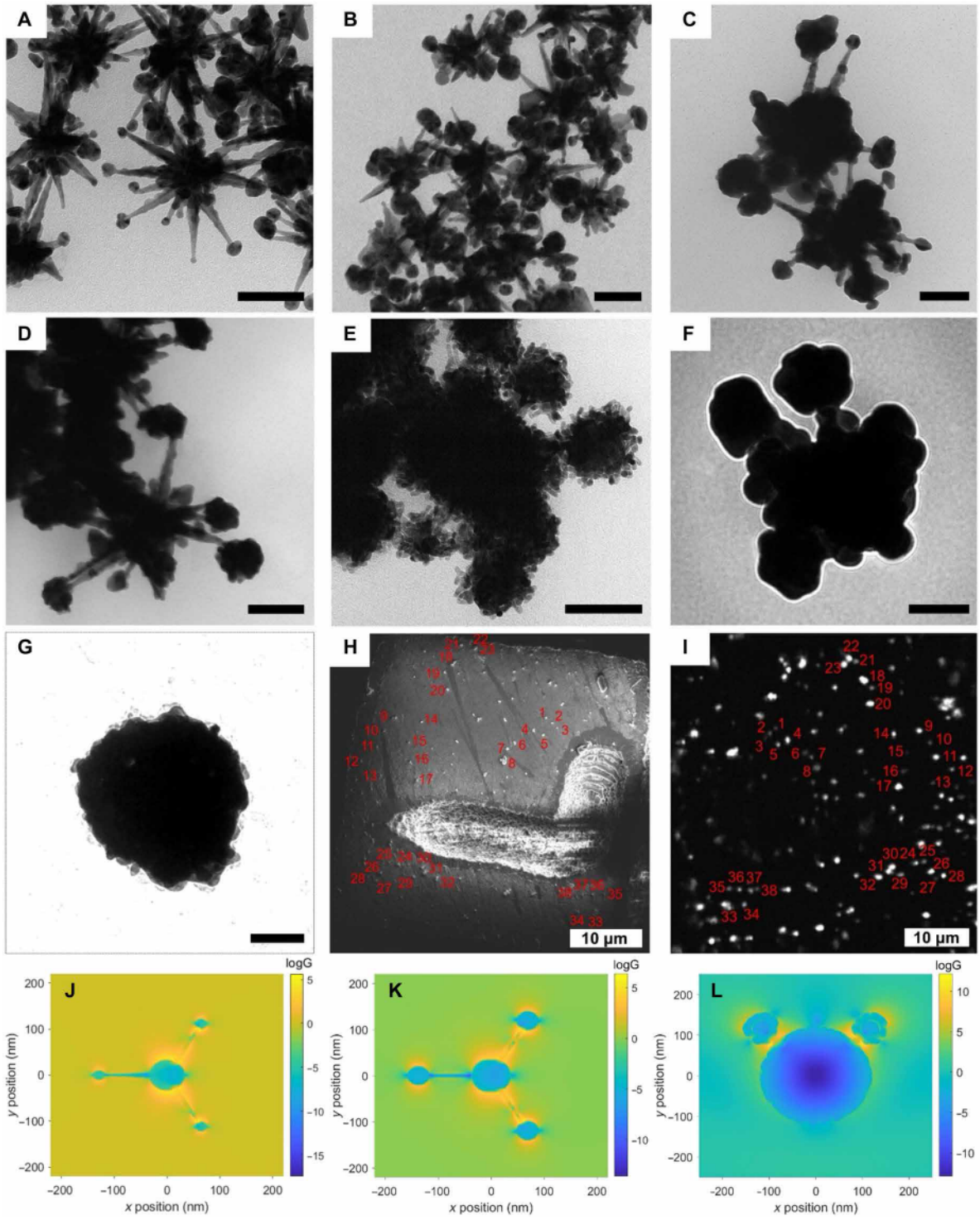

Fig. 4. Star-core CS NP synthesis, SECARS measurement, and simulations. Star-core CS NP synthesized using a linker-free method. (**A**) CS NPs (8 ml of seed solution), (**B**) CS NPs (4 ml of seed solution), (**C**) CS NPs (2 ml of seed solution), (**D**) CS NPs (1 ml of seed solution), (**E**) CS NPs (0.5 ml of seed solution), (**F**) CS NPs (0.25 ml of seed solution), and (**G**) CS NPs (0.125 ml of seed solution). Scale bars, 100 nm. (**H**) SEM image of letter "L" on the photoetched glass substrate with labeled grids, on which CS NPs [0.25 ml of seed solution; NP in (F)] spread. (**I**) The averaged SECARS image of a hyperspectral imaging stack that covered the same ROI of (H). The total EFs [$G = g_p^4 g_s^2 g_{as}^2$; g_p, g_s, and g_{as}: EF at the wavelengths of pumping (912 nm), Stokes (1040 nm), and anti-Stokes (812 nm)] are presented for (**J**) CS NP [4 ml of seed solution; NP in (B)], (**K**) CS NP [2 ml of seed solution; NP in (C)], and (**L**) asymmetric CS NP [0.25 ml of seed solution; NP in (F)].